Mapping the orientation of nuclear pore proteins in living cells with polarized fluorescence microscopy

Martin Kampmann[1,2,4], Claire E Atkinson[3], Alexa L Mattheyses[3,4] & Sanford M Simon[3]

The nuclear pore complex (NPC) perforates the nuclear envelope to facilitate selective transport between nucleus and cytoplasm. The NPC is composed of multiple copies of ~30 different proteins, termed nucleoporins, whose arrangement within the NPC is an important unsolved puzzle in structural biology. Various alternative models for NPC architecture have been proposed but not tested experimentally in intact NPCs. We present a method using polarized fluorescence microscopy to investigate nucleoporin orientation in live yeast and mammalian cells. Our results support an arrangement of both yeast Nic96 and human Nup133–Nup107 in which their long axes are approximately parallel to the nuclear envelope plane. The method we developed can complement X-ray crystallography and electron microscopy to generate a high-resolution map of the entire NPC, and may be able to monitor nucleoporin rearrangements during nucleocytoplasmic transport and NPC assembly. This strategy can also be adapted for other macromolecular machines.

Understanding the mechanism of large macromolecular complexes is greatly facilitated by detailed knowledge of their structure. The elucidation of high-resolution structures of large complexes presents a unique challenge: high-resolution techniques, namely X-ray crystallography, can typically be applied only to individual proteins or smaller subcomplexes; conversely, techniques that are suitable for the study of the entire assembly, such as electron microscopy (EM), have limited resolution. Hence, structural information obtained from different techniques has to be integrated, which can be a formidable problem when the resolution gap between different types of structures is wide.

A prime example of a macromolecular assembly that poses such a 'resolution-gap' problem is the nuclear pore complex (NPC), which mediates transport between the nucleus and the cytoplasm of eukaryotic cells (see ref. 1 for a recent review). The NPC is embedded in nuclear envelope pores and has a total mass of ~50 MDa in budding yeast and ~120 MDa in vertebrates. It is composed of ~30 distinct proteins, termed nucleoporins, which occur in multiple copies per NPC.

The structure of the NPC has been studied with different experimental approaches. EM has revealed the overall shape and symmetry of the NPC. Cryoelectron tomography has provided snapshots at a resolution better than 6 nm (ref. 2). X-ray crystallography has elucidated high-resolution structures of an increasing number of individual nucleoporins and of some binary and ternary nucleoporin complexes[3]. However, the resolution of structures of the entire NPC is currently not sufficient to relate high-resolution nucleoporin structures to the whole NPC by molecular docking. One approach to bridging this resolution gap is three-dimensional EM of NPC subcomplexes, followed by docking of nucleoporin crystal structures into the subcomplex EM map. This strategy has revealed the arrangement of seven nucleoporins within the Y-shaped Nup84 subcomplex[4]. However, this approach has not yet resolved the higher-order arrangement of the Y-shaped subcomplex within the NPC.

For the reasons described above, the arrangement and orientation of nucleoporins within the NPC is unknown. Several models for the arrangement of nucleoporins have been suggested. On the basis of immuno-EM and protein-protein interaction data, a coarse model for NPC architecture has been generated computationally[5]. However, this model lacks information regarding the orientation of NPC building blocks, which would be required for the docking of crystal structures into the overall map. On the basis of crystal structures and biochemical data, models have been proposed for the arrangement of two NPC building blocks, Nic96 and the Y-shaped subcomplex. For Nic96, an octameric ring arrangement has been proposed, in which the long axis of Nic96 is perpendicular to the nucleocytoplasmic axis[6]. For the Y-shaped subcomplex, two mutually exclusive models have been proposed: the 'lattice' model[7,8], in which the complex is arranged around the NPC like a picket fence, and the 'head-to-tail ring' model[9–11], in which the complex forms a ring around the pore. These models differ in the orientation of the Y-shaped subcomplex within the NPC. More generally, knowledge of the orientation of different nucleoporins within the NPC is essential to determining the details of NPC architecture.

An experimental approach to mapping the orientation of nucleoporins within the NPC, either *in vitro* or *in vivo*, has not been described thus far. Here, we present a method for orientation mapping of nucleoporins in live yeast and mammalian cells using polarized fluorescence microscopy. Polarized fluorescence microscopy has previously been used to investigate macroscopically ordered systems of different geometries[12–17]. In particular, the anisotropy measured

[1]Laboratory of Cell Biology, The Rockefeller University, New York, New York, USA. [2]Howard Hughes Medical Institute, Chevy Chase, Maryland, USA. [3]Laboratory of Cellular Biophysics, The Rockefeller University, New York, New York, USA. [4]Present addresses: Department of Cellular and Molecular Pharmacology and Howard Hughes Medical Institute, University of California at San Francisco, San Francisco, California, USA (M.K.), Department of Cell Biology, Emory University School of Medicine, Atlanta, Georgia, USA (A.L.M.). Correspondence should be addressed to martin.kampmann@ucsf.edu or simon@rockefeller.edu.
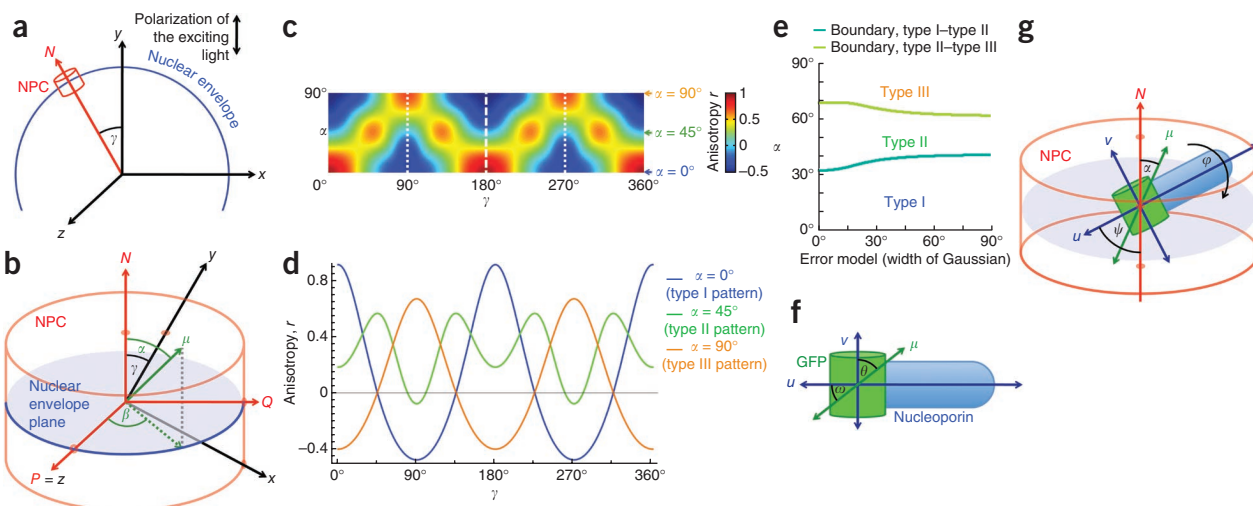
Figure 1 Fluorescence anisotropy patterns reflect the orientation of fluorophores within the NPC. (**a**) A circular nuclear envelope cross-section seen in the microscope coordinate system *xyz*. The polarization direction of the exciting light is parallel to *y*. The object plane is defined by *xy*, the optical axis by *z*. The nucleocytoplasmic axis *N* of each NPC is perpendicular to the plane tangential to the point in the nuclear envelope at which the NPC is located. The angle between the *y* axis and *N* at a given point in the nuclear envelope is defined as *γ*. (**b**) An individual NPC with its own coordinate system *NPQ*. *P* is chosen to coincide with the optical axis *z*, *PQ* defines the nuclear envelope plane. The transition dipole of a fluorophore fixed within the NPC is *μ*. The orientation of *μ* within the NPC is described by *α*, the angle between *μ* and *N*, and *β*, the angle between *P* and the projection of *μ* onto the nuclear envelope plane *PQ*. (**c**) For a fluorophore with a given angle *α*, the anisotropy *r* can be predicted as a function of the nuclear envelope position *γ*. All functions *r*(*γ*) have a period of 180° (dashed line) and have mirror symmetry axes (dotted lines). (**d**) Anisotropy patterns along the nuclear envelope cross-section are shown for three values of *α* that exemplify different pattern types, as defined in the text. (**e**) The values of *α* at which transitions between pattern types occur were plotted as a function of the width of the Gaussian function with which the theoretical anisotropy pattern was convoluted to approximate the effect of experimental factors on the measured anisotropy values (see **Supplementary Note**). (**f**) Two perpendicular axes, *u* and *v*, are arbitrarily defined within the nucleoporin. For a given nucleoporin-GFP construct, the angle between *u* and the fluorophore transition dipole *μ* is designated *ω*; and the angle between *v* and *μ* is *θ*. (**g**) The orientation of a nucleoporin within the NPC is characterized by two parameters: *ψ*, the angle between *u* and the nucleocytoplasmic axis *N*, and *φ*, the angle of rotation around *u*.

from a rigid tagging of green fluorescent protein (GFP) was used to monitor the orientation of septins in yeast cells[15,16]. We have recently used polarized fluorescence microscopy to probe the flexibility of nucleoporin domains in live cells[18].

We adapted and further developed these strategies to interpret information from polarized fluorescence microscopy in combination with known crystal structures of nucleoporins. Using this approach, we obtained results that confirm the consensus model[6] for the arrangement of Nic96 in the budding yeast NPC and support the head-to-tail ring model but not the lattice model for the 'Y-shaped' subcomplex in human cells. Although designed to measure nucleoporin orientation, this method can also be applied to investigate other protein assemblies in live cells.

RESULTS
Anisotropy patterns from NPC–fixed fluorophores
We set out to use polarized fluorescence microscopy to map the orientation of nucleoporins within the NPC. First, we derived an analytical description of how the variation in the anisotropy of a fluorescently tagged nucleoporin around the nuclear envelope depends on the orientation of the nucleoporin within the NPC. We defined a microscope-based coordinate system *xyz* such that *z* corresponds to the optical axis and *yz* to the plane of polarization of the exciting light (**Fig. 1a**). We then defined an NPC-based coordinate system *NPQ* such that *N* is the nucleocytoplasmic axis and eight-fold symmetry axis of an individual NPC, and *P* and *Q* are parallel to the surrounding nuclear envelope; we chose *P* to coincide with *z* (**Fig. 1b**). When the cross-section of a spherical yeast nucleus is imaged by microscopy, the angle *γ* between *N* and *y* varies along the nuclear envelope cross-section (**Fig. 1a**). When a fluorophore is rigidly attached to a structured nucleoporin, the orientation of its transition dipole *μ* is characterized

by the angle *α* between *N* and *μ* (**Fig. 1b**). Owing to the symmetry constraints of the NPC, GFP molecules attached to nucleoporins that are present in 8 or 16 copies per NPC differ in their position around *N* (as indicated by angle *β*), but they all share the same *α*.

Next, we calculated how *α* determines the pattern of anisotropy, a measure of the polarization of light. Anisotropy is defined as:

$$r = \frac{I_{\parallel} - I_{\perp}}{I_{\parallel} + 2I_{\perp}} \tag{1}$$

where $I_{\parallel}$ is the component of emitted light polarized parallel to the polarization of the exciting light, and $I_{\perp}$ is the perpendicular component. In the case of fluorophores attached to the NPC, the anisotropy will vary around the nuclear envelope cross-section as follows:

$$r(\gamma) = (K_2 - K_1)\frac{I_y - I_x}{(K_1 + 2K_2)I_x + (K_2 + 2K_1)I_y + 3K_3 I_z} \tag{2}$$

where

$$I_x = \tfrac{1}{2}a^2 c^2 + a^2 d^2 + \tfrac{3}{8}b^2 c^2 + \tfrac{1}{2}b^2 d^2 - 2abcd \tag{3}$$

$$I_y = a^4 + 3a^2 b^2 + \tfrac{3}{8}b^4 \tag{4}$$

$$I_z = \tfrac{1}{2}a^2 \sin^2 \alpha + \tfrac{1}{8}b^2 \sin^2 \alpha \tag{5}$$

and $a = \cos\alpha\cdot\cos\gamma$, $b = \sin\alpha\cdot\sin\gamma$, $c = \sin\alpha\cdot\cos\gamma$ and $d = \cos\alpha\cdot\sin\gamma$.

Our derivation of equations (2–5) is given in the **Supplementary Note**. K_1, K_2 and K_3 are correction factors for the high-numerical-aperture observation[13]. Equation (2) is shown in **Figure 1c**. As expected from the symmetry of the NPC–nuclear envelope system, *r*(*γ*) has a periodicity of 180° and shows mirror symmetry around the axes *γ* = 90°, *γ* = 180° and *γ* = 270°.

Although experimentally measured anisotropy values differ from the theoretical values (**Supplementary Note**), the overall anisotropy

Figure 2 Nic96-GFP constructs with a continuous linker α-helix. Sequences of the budding yeast Nic96 C terminus (blue) and of the GFP N terminus (green) are shown with α-helical segments underlined. The C-terminal α-helix of Nic96 can be fused to the N-terminal α-helix of GFP such that a continuous linker helix connects the two moieties. Models of fusion proteins based on crystal structures of Nic96 (light blue) and GFP (green, with fluorophore in orange) are shown.

pattern is less sensitive to experimental factors. Three types of anisotropy patterns are predicted (**Fig. 1d**): type I, showing maxima for $\gamma = 0°$ and 180° and minima for $\gamma = 90°$ and 270°; type II, showing minima for $\gamma = 0°$, 90°, 180° and 270°, alternating with maxima; type III, with minima for $\gamma = 0°$ and 180° and maxima for $\gamma = 90°$ and 270°.

The α-values at which transitions between pattern types occur are shown in **Figure 1e**. The dependence on α is relatively robust with respect to experimental error. Photobleaching does not affect anisotropy measurements in our setup (**Supplementary Fig. 1a**); however, experimental factors affecting the measured anisotropy values include the resolution of the microscope in the z-direction, averaging of pixels with different γ-values during image processing, and fluorophore flexibility. These experimental factors cause flattening of the measured anisotropy curves (**Supplementary Note**), which can be approximated by convolution of the theoretical anisotropy curves with a Gaussian function (**Supplementary Fig. 1b**). The exact width of this Gaussian function is unknown, but over the range of widths tested, even very wide Gaussian functions changed the boundaries between pattern types only over a narrow range of α-values (**Fig. 1e**). Therefore, we can make the following very conservative assumptions about α based on the observed pattern type: type I: $0° \leq \alpha < 42°$; type II: $33 \leq \alpha \leq 68°$; type III: $60° < \alpha \leq 90°$.

The amplitude of $r(\gamma)$ within one pattern type changes monotonically with α. Hence, when comparing two anisotropy patterns of the same type with different amplitudes, acquired for different nucleoporin-fluorophore constructs under the same experimental conditions, it is always possible to determine which construct has a relatively higher α value.

In summary, we can gain information about the orientation of the dipole of a fluorophore fixed within the NPC by examining the pattern of anisotropy maxima and minima around the nuclear envelope cross-section. However, the biological parameter of interest is the orientation of nucleoporins within the NPC, and not the orientation of the fluorophore itself. The spatial relation of a fluorophore to a nucleoporin can be formalized as shown in **Figure 1f**: two perpendicular axes u and v are arbitrarily defined within the nucleoporin. ω and θ are the angles between μ and u, and μ and v, respectively. The orientation of the nucleoporin within the NPC is characterized by two angles (**Fig. 1g**): ψ, the angle between u and N, and φ, which describes the rotation of v around u. We show below how to derive information about ψ and φ from anisotropy patterns.

Functional Nic96-GFP fusion proteins with known geometry

To map the orientation of nucleoporin-GFP fusion constructs within the NPC, rigid constructs with known geometry are required. To this aim, we adapted a previously published approach[15]. GFP contains a short N-terminal α-helix, which can be fused directly to a C-terminal α-helix in a protein of interest, to link the two proteins by a continuous α-helix. When the number of amino acids in this linker helix is varied, GFP rotates around the linker helix axis by angles dictated by α-helical geometry[16]. For GFP, the orientation of the fluorescence transition dipole relative to its crystal structure has already been determined[19]. Therefore, the orientation of the dipole with respect to the nucleoporin can be predicted based on the length of the linker helix. In our nomenclature,
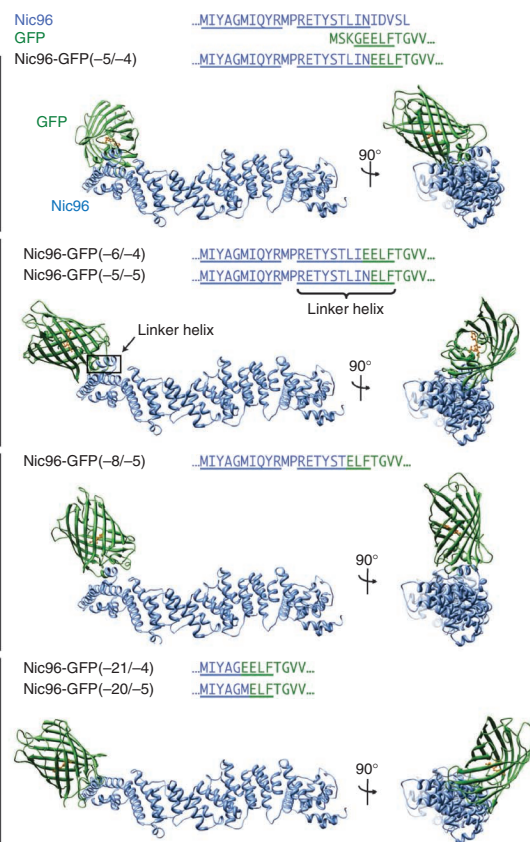
a fusion construct is described by the two numbers $-p$ and $-q$ (denoted below as $-p/-q$), indicating the number of amino acids omitted from the C terminus of the nucleoporin (p) and the number of amino acids omitted from the N terminus of GFP (q). Different constructs for which the sum of p and q is the same have a linker helix of the same length.

The first nucleoporin we chose to investigate was yeast Nic96, because a model has been proposed for its orientation in the NPC[6], which makes Nic96 a good test case for our method. Nic96 contains C-terminal α-helices, and crystal structures for its C-terminal domain are available[6,20], which allowed us to generate molecular models for Nic96-GFP fusion constructs (**Fig. 2**). Because Nic96 is an essential protein in yeast, we were able to assay whether a given Nic96-GFP construct was functional *in vivo* (**Supplementary Fig. 2a**). Molecular models for some nucleoporin-GFP fusion constructs contain internal steric clashes between the nucleoporin and GFP moieties (red stars in **Supplementary Fig. 2a**). These constructs therefore cannot exist in the modeled conformations, and when they were expressed in yeast, they showed reduced or no functionality, as assayed by tetrad analysis, and the GFP fluorescence lacked a clear nuclear localization (**Supplementary Fig. 2**). These constructs, as well as other constructs with drastically reduced Nic96 function and/or reduced nuclear-envelope staining, were excluded from further analysis. The six Nic96-GFP constructs that passed all tests were (−5 /−4), (−6 /−4), (−5 /−5), (−8 /−5), (−21 /−4) and (−20 /−5).

Anisotropy patterns support model for Nic96 arrangement

We collected $I_{\parallel}$ and $I_{\perp}$ images of GFP-labeled cells in parallel, using an optimized microscope setup (details are described in the Online Methods section). To calculate accurate anisotropy values pixel by pixel, precise alignment of the $I_{\parallel}$ and $I_{\perp}$ images was necessary, especially because the nuclear envelope signal was only a few pixels wide.
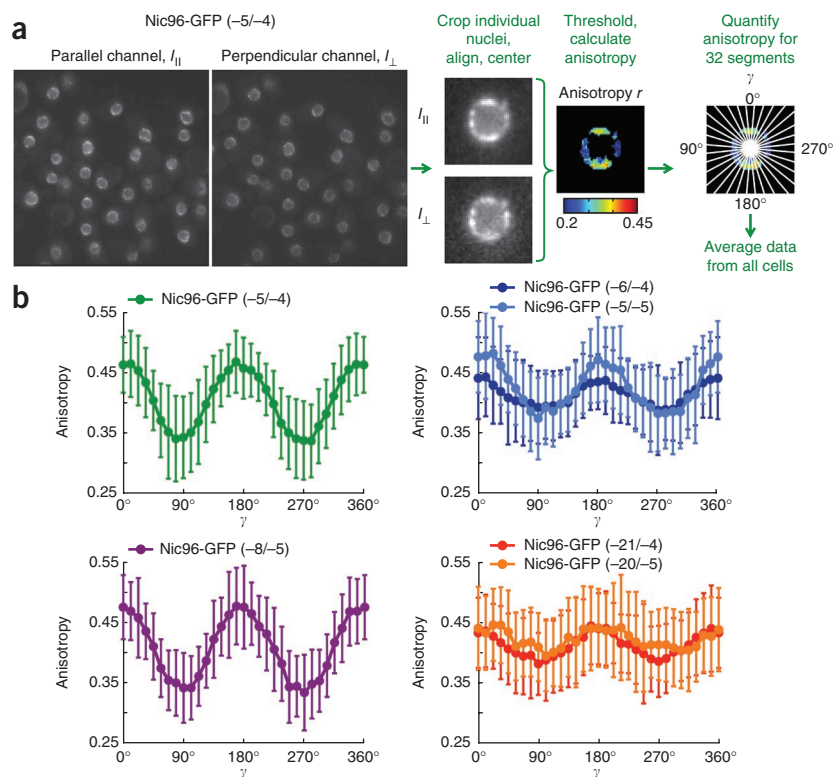
Figure 3 Polarized fluorescence microscopy reveals anisotropy patterns for yeast strains expressing Nic96-GFP constructs. (**a**) GFP-tagged yeast cells are excited with polarized light. Parallel and perpendicular components of the emitted light, $I_{||}$ and $I_{\perp}$, are recorded simultaneously. Images of individual nuclei are cropped from the background-corrected micrographs and processed automatically as follows: $I_{||}$ and $I_{\perp}$ images of the same nucleus are aligned and centered, and pixels not belonging to the nuclear envelope are masked by thresholding. An anisotropy image is calculated, and the average anisotropy is calculated within 32 sectors. (**b**) Experimental anisotropy curves for six Nic96-GFP constructs. Error bars represent the s.d. of average sector anisotropy values from at least 75 individual cells per construct.

Global alignment of the $I_{||}$ and $I_{\perp}$ halves of the micrograph did not give satisfactory results for all cells. We therefore cropped image pairs of individual nuclei from the micrographs (**Fig. 3a**) and aligned all image pairs automatically with sub-pixel accuracy based on their cross-correlation. Intensity-based thresholding of each image pair to exclude pixels that did not represent the nuclear envelope was also more accurate on a nucleus-by-nucleus basis. We automatically centered the nucleus within the image, using a center-of-gravity algorithm, and calculated the anisotropy image from background-corrected, aligned $I_{||}$ and $I_{\perp}$ images. The anisotropy image was divided into 32 segments and the values within each segment were recorded (**Fig. 3a**).

The resulting anisotropy patterns were averaged over all nuclei (**Fig. 3b**). All patterns were type I, but the amplitudes of the (−5/−4) and (−8/−5) patterns were higher than those of the other patterns. Although in the case of the Nic96-GFP constructs all patterns were type I, this was not true of all yeast nucleoporins. A series of Nup84-GFP constructs showed a different combination of pattern types (**Supplementary Fig. 3**).

To interpret the anisotropy measurements for Nic96-GFP constructs, we defined axes u and v within Nic96 (**Fig. 4a**). The u axis corresponds to the long axis of the crystallized Nic96 domain. Because constructs (−6 /−4) and (−5 /−5) have the same linker helix length, as do constructs (−21 /−4) and (−20 /−5), we generated four distinct molecular models for the six constructs (**Fig. 2**). From each model, we determined angles θ and ω. This allowed us to calculate for each construct the value of α expected for any combination of ψ and φ (**Fig. 4b**, first row) (see **Supplementary Note** for details).

We then used these construct-specific plots of α as a function of ψ and φ to identify the range of ψ and φ values that was compatible with the anisotropy patterns we observed. As described in the previous section, our conservative assumption is that type I anisotropy patterns occur for constructs with $\alpha < 42°$. Because we observed type I patterns for all constructs, we could restrict the space of possible ψ and φ combinations in each plot to those values that correspond to $\alpha < 42°$ (**Fig. 4b**, second row).

We were able to further define possible ψ and φ combinations by comparing the amplitudes between pairs of anisotropy patterns for the different constructs (**Fig. 4b**, third row). For two constructs with type I patterns, the construct with the higher amplitude will have the lower value of α. For example, the amplitude for Nic96-GFP (−5/−4) was larger than that for Nic96-GFP (−6/−4), Nic96-GFP (−5/−5), Nic96-GFP (−21/−4) and Nic96-GFP (−20/−5). Therefore, only combinations of ψ and φ for which Nic96-GFP (−5/−4) had smaller α-values than the other four constructs were compatible with our data.

By combining all these conditions, we can restrict ψ to values between 77° and 90° and φ to values between 20° and 45° (**Fig. 4b**, bottom row). Notably, the high value of ψ indicates that the long axis of Nic96 is approximately perpendicular to the nucleocytoplasmic axis of the NPC (**Fig. 4c**), as predicted by the published model for the arrangement of Nic96 within the NPC[6].

To validate our method, we applied it to a different biological system, the vacuolar ATPase complex. This protein complex is embedded in the membrane of the yeast vacuole, a large, spherical organelle. The vacuolar ATPase complex–vacuolar membrane system and the NPC–nuclear envelope system thus have similar geometries. GFP-tagging of a vacuolar ATPase subunit with known orientation resulted in the anisotropy pattern that our theory predicted (**Supplementary Fig. 4**), thus confirming the general applicability of our approach.

Nup133-GFP supports Y-shaped complex head-to-tail ring

A question of considerable biological interest is the orientation of the Y-shaped subcomplex within the NPC[7–11]. We decided to study the Y-shaped subcomplex from mammalian cells (the Nup107–Nup160 complex), rather than the homologous subcomplex from yeast (the Nup84 complex), because no crystal structure containing a C-terminal α-helix is currently available for members of the yeast Y-shaped complex. Structures of the C-terminal domains of two members of the human Y-shaped complex, Nup107 and Nup133, have been published[21–23]. Several of the Nup133-GFP constructs we tested (**Supplementary Fig. 5**) localized to the nuclear envelope in HeLa cells (**Fig. 5a**), whereas none of the Nup107-GFP constructs did.

Although anisotropy patterns can be observed for Nup133-GFP constructs in individual HeLa cells (**Fig. 5b**), our algorithm for automated quantification of r as a function of γ had to be modified from the yeast algorithm, because nuclei of mammalian cells are not as spherical as

Figure 4 Analysis of anisotropy patterns reveals approximate orientation of Nic96 within the NPC. (**a**) Two axes are defined with respect to the crystallized domain of Nic96, the long axis u and a perpendicular axis v. (**b**) First row: for each Nic96-GFP construct, θ and ω are derived from the molecular model. α is calculated for all possible combinations of ψ and φ. Second row: the experimental anisotropy patterns (**Fig. 3b**) were all type I, corresponding to a value of $\alpha < 42°$. Combinations of ψ and φ values satisfying this condition are shown in white; incompatible combinations of ψ and φ are shown in black. Third row: because the amplitude of type I patterns decreases as α increases between 0° and 42°, pairwise comparison of anisotropy curves with different amplitudes (**Fig. 3b**) further restricts the space of possible combinations of ψ and φ. Last row: all restrictions are combined to reveal the remaining space of possible ψ and φ values (white). (**c**) A value of ψ close to 90° is compatible with a published model[6] in which Nic96 molecules were proposed to form a ring with their long axes perpendicular to the nucleocytoplasmic axis, as shown schematically here.

yeast nuclei. We cropped small regions of quasilinear nuclear envelope segments from each micrograph (**Fig. 5c**) and determined the orientation of each segment automatically by cross-correlation–based matching between the experimental image and synthetic template images representing orientations of γ between 0° and 180° in 10° increments (**Fig. 5d**). We calculated the average anisotropy as for yeast cells, and plotted anisotropy graphs (**Fig. 5e**). The experimental anisotropy graphs for mammalian cells cover a range of 0° < γ < 180°, which is sufficient to interpret the anisotropy pattern, due to the 180° periodicity of $r(\gamma)$.

We analyzed four Nup133-GFP constructs for which the molecular models showed no internal steric clashes (**Supplementary Fig. 5**). Constructs (−2/−5) and (−3/−4) have a linker helix with the same length, as do constructs (−3/−5) and (−4/−4). Constructs (−2/−5) and (−3/−4) showed a type I anisotropy pattern. The anisotropy curves for constructs (−3/−5) and (−4/−4) are relatively noisy, but the presence of a clear maximum at $\gamma = 90°$ is the hallmark of a type III anisotropy pattern (compare to **Fig. 1d**).

Based on the structure of a complex between the C-terminal domains of Nup107 and Nup133, we defined u as the axis between the N-terminal residues of the Nup107 and Nup133 constructs, thus pointing toward the remaining residues of the two nucleoporins (**Fig. 6a**). On the basis of the structure of the homologous yeast Nup84 complex[4], we assume that Nup107 and Nup133 are arranged linearly
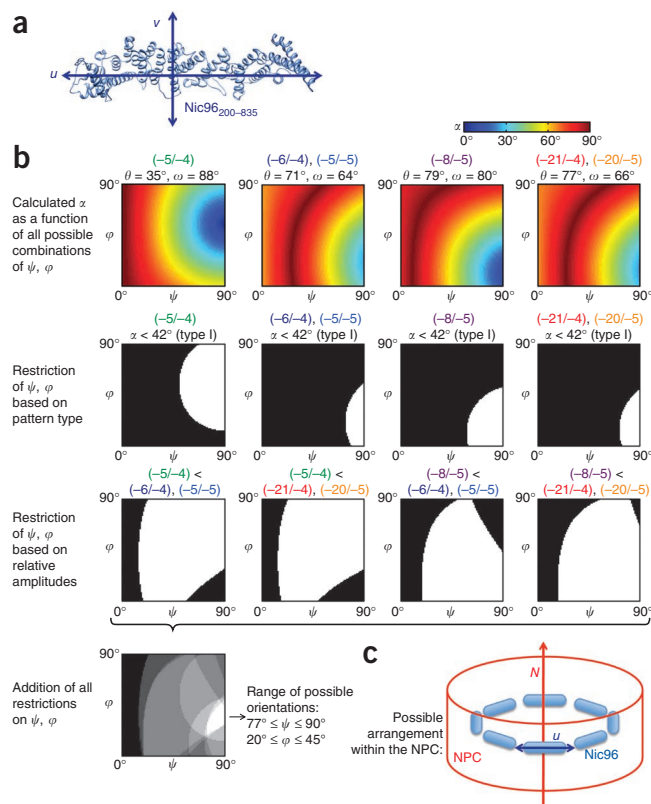
along the stem of the Y-shaped subcomplex. Hence, u is likely to reflect the orientation of the stem of the Nup107 complex.

We created maps of α as a function of φ and ψ for the Nup133-GFP constructs (**Fig. 6b**, first row) as described for the yeast constructs. On the basis of the observed anisotropy patterns, our conservative assumptions were $\alpha < 42°$ for constructs (−2/−5) and (−3/−4) (type I pattern) and $\alpha > 60°$ for constructs (−3/−5) and (−4/−4) (type III pattern) (**Fig. 6b**, second row). These conditions restricted ψ to values between 76° and 90° and φ to values between 36° and 90° (**Fig. 6b**, bottom row), indicating that the long axis of the Nup107–Nup133 dimer, which is likely to represent the stem axis of the entire subcomplex, lies approximately perpendicular to the nucleocytoplasmic axis of the NPC. Such an arrangement is compatible with the head-to-tail ring model, in which the Y-shaped subcomplexes lie with their long axes parallel to the nuclear envelope plane and form a ring through interaction of the end of the stem of the 'Y' with the short arms of the neighboring 'Y'[9] (**Fig. 6c** and **Supplementary Fig. 6a**). However, the anisotropy patterns are not compatible with the lattice model as originally proposed, or with any other models in which the Y-shaped subcomplexes interact
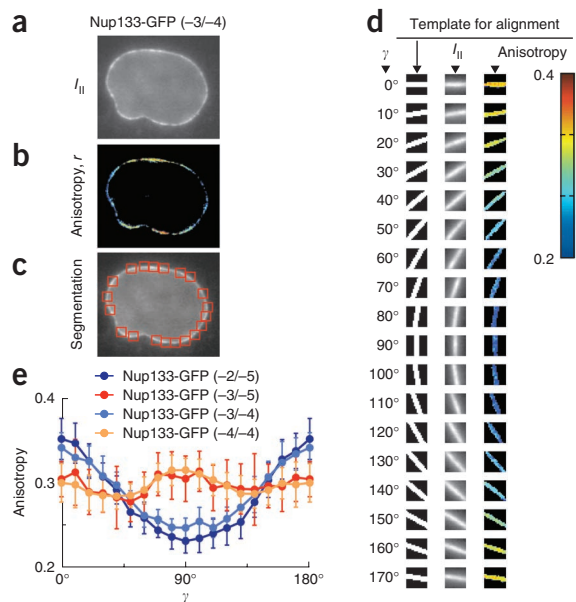

Figure 5 Anisotropy patterns in mammalian cells expressing Nup133-GFP. (**a**) $I_{||}$ image from polarized fluorescence microscopy of HeLa cell expressing Nup133-GFP (−3/−4). (**b**) Pseudocolored anisotropy image of the same cell. (**c**) 16 × 16 pixel boxes containing quasi-straight segments of nuclear envelope are selected. (**d**) Cross-correlation between the nuclear envelope segment and a series of template images is calculated to match the experimental image with the most similar template and thus to determine the orientation of the nuclear envelope segment. First column, γ values; second column, corresponding synthetic template images; third column, average $I_{||}$ images of aligned segments from all Nup133-GFP (−3/−4) cells; fourth column, averaged anisotropy images of these segments. (**e**) Anisotropy curves obtained from segment analysis as outlined in **d**, for four different Nup133-GFP constructs. Error bars represent the s.d. of average segment anisotropy values from ~25 individual boxes per construct.

Figure 6 Nup133-GFP anisotropy patterns are consistent with the published 'head-to-tail ring' arrangement of the Y-shaped subcomplex. (**a**) Two axes are defined with respect to the Nup133–Nup107 dimer: the long axis u connects the N termini of the crystallized Nup107 and Nup133 domains, which connect to the remaining parts of the stem of the Y-shaped subcomplex. u should correspond approximately to the long axis of the entire subcomplex. The perpendicular axis v passes through the Nup133 C terminus. (**b**) First row: for each Nup133-GFP construct, α was calculated for all possible combinations of ψ and φ. Second and last rows: for constructs (−3/−4) and (−2/−5), type I anisotropy patterns were observed (**Fig. 5e**), indicating $\alpha < 42°$; for constructs (−4/−4) and (−3/−5), the type III anisotropy patterns were observed (**Fig. 5e**), indicating $\alpha > 60°$. Combinations of ψ and φ compatible with these restrictions are shown in white. (**c**) The anisotropy data indicate that the angle ψ between u, the long axis of the Nup107–Nup133 complex and the nucleocytoplasmic axis N is closer to 90° than to 0°. This supports a model for the arrangement of the entire Y-shaped subcomplex in flat octameric head-to-tail rings. For illustrative purposes, one such model was generated using the EM map of the homologous yeast Y-shaped complex and represents one subcomplex ring viewed along N. Colors indicate building blocks of the Y-shaped subcomplex. Additional details are given in **Supplementary Figure 6**.
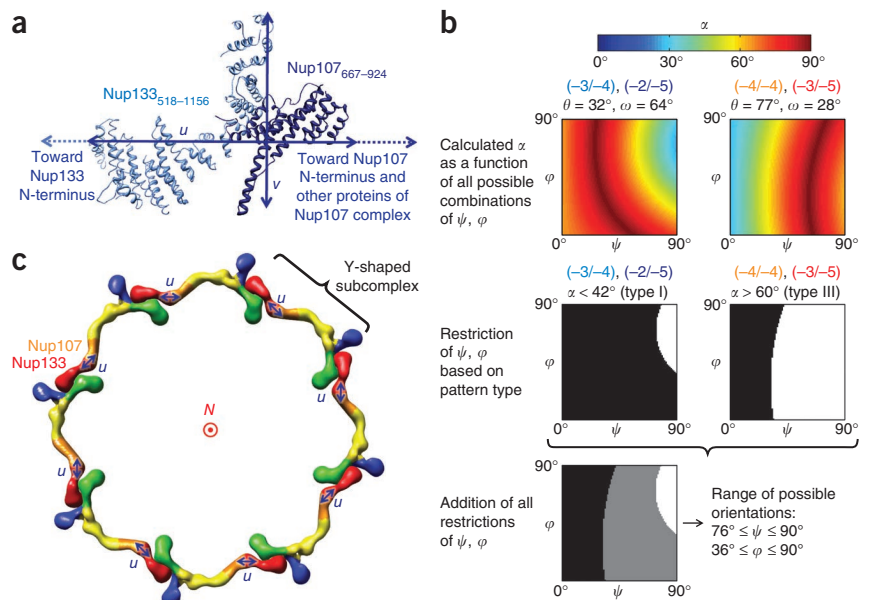
via their short arms, with their long axes parallel to the nucleocytoplasmic axis[8] (**Supplementary Fig. 6b**). The same answer is obtained by asking which anisotropy pattern types we would expect to observe on the basis of the alternative models for the arrangement of the Y-shaped complex in the NPC (**Supplementary Fig. 6d**).

DISCUSSION

We have developed a method to map the orientation of nucleoporins within the NPC of live yeast and mammalian cells. The development of this method required us to address several technical challenges. To acquire micrographs with a sufficient signal-to-noise ratio despite the low abundance of nucleoporins in yeast, we optimized cell culture conditions to minimize cellular background fluorescence. In addition, we computationally corrected for the remaining background fluorescence. To cleanly separate $I_\parallel$ and $I_\perp$ light components, we customized our microscope setup using a laser, a half-wave plate and clean-up polarizers. To align $I_\parallel$ and $I_\perp$ images with sub-pixel accuracy, we developed a cross-correlation–based algorithm.

Several caveats in the interpretation of anisotropy patterns needed to be considered. First, as in all GFP-tagging experiments, a primary concern was that the GFP tag could disrupt the structure and localization of the tagged protein. To exclude such disruptive nucleoporin-GFP constructs from our analysis, we applied a combination of three criteria to each construct in yeast: (i) the molecular model of the nucleoporin-GFP construct had to be free of steric clashes, (ii) the construct needed to show a robust nuclear envelope localization *in vivo*, and (iii) the nucleoporin-GFP had to be functional *in vivo*. In the case of an essential nucleoporin, such as Nic96, viability of cells in which Nic96-GFP replaces wild-type Nic96 can directly be assayed (**Supplementary Fig. 2a**). For nonessential nucleoporins, the functionality of the fusion construct can be assayed in a genetic background lacking a second gene that is synthetic lethal with the nucleoporin of interest. We found that the three criteria above were correlated for most Nic96-GFP constructs (**Supplementary Fig. 2**). Only constructs satisfying all three criteria were used for further analysis. The first two criteria were applied to mammalian cells as well.

A second caveat is the experimental error in the anisotropy values (discussed in the **Supplementary Note**). We overcame this issue by relying on anisotropy pattern types, rather than absolute anisotropy values, for our analysis. Our conclusions based on anisotropy patterns were extremely conservative (**Supplementary Note**), yet they efficaciously restricted the space of possible nucleoporin orientations (**Figs. 4** and **6**). The results from all of the nucleoporin-GFP constructs we investigated were consistent with each other, which supports the validity of our approach.

The third caveat is that the *in vivo* conformation of a nucleoporin-GFP fusion construct may differ from the conformation predicted by the molecular model. Although short α-helices are very stiff in isolation (persistence length ~100 nm, ref. 24), interactions with other molecular surfaces in the NPC may bend the linker helix. This possibility is difficult to exclude experimentally, because even a crystal structure of the nucleoporin-GFP construct may not reflect the geometry adopted in the context of the NPC. However, our results support the conclusion that the molecular model was generally an adequate description of the nucleoporin-GFP geometry: (i) different constructs with the same linker helix length, and thus the same predicted geometry, produced indistinguishable anisotropy patterns; a small divergence was observed only in the cases of Nic96-GFP (−5/−5) and (−6/−4). (ii) Conclusions from all individual constructs were consistent with each other; anisotropy patterns never resulted in mutually exclusive predictions of φ and ψ. (iii) Models derived from our analysis are consistent with NPC dimensions. In particular, the conclusion that the long axis of the Y-shaped subcomplex is close to perpendicular to the nucleocytoplasmic axis is compatible with the size of the central NPC, whereas an arrangement of the subcomplex with its long axis (~45 nm long[4]) parallel to the nucleocytoplasmic axis would exceed the height of one half of the central NPC (~15–20 nm, ref. 2). (iv) Models that did not show steric clashes both localized properly at the nucleus and could complement the loss of the endogenous gene, whereas this was not true of those constructs that were predicted to contain a steric clash. The fact that yeast cells expressing nucleoporin-GFP constructs with predicted steric clashes possessed generally reduced viability supports the idea that the structure of the

fusion construct is rather rigidly dictated by the nucleoporin–GFP linkage, and is not easily altered by other external factors.

The method we describe here can be applied to all nucleoporins that feature an α-helical C-terminal domain. According to secondary structure predictions, ~60% of nucleoporins meet this requirement[25]. Although it should be possible to collect anisotropy data for all of these nucleoporins, the derivation of orientation information from the anisotropy patterns will require a solved crystal structure of the C-terminal domain. If the elucidation of nucleoporin crystal structures progresses at the current pace[3], our method should help to map the orientation of most NPC components over the next few years. Our experimental determination of nucleoporin orientations will complement crystallographic and EM data to aid in the construction of a high-resolution map of the entire NPC, which will be the basis of a detailed mechanistic understanding of the NPC.

Because the present method is applied to live cells, it can be used to monitor changes in nucleoporin orientation that correlate with NPC assembly and transport. Structural studies suggest that even the ordered components of the NPC are highly dynamic[2,4,26], but the biological significance of this flexibility is unclear, because it has not been studied in intact cells. Using small-molecule inhibitors of nucleocytoplasmic transport or temperature-sensitive transport mutants, NPCs can be arrested in an inactive state[27], and nucleoporin orientations in the inactive state can be compared to those in the active state to reveal conformational changes that occur specifically during active transport. Time-resolved studies of NPC assembly can yield insights into nucleoporin rearrangements during the assembly process.

Finally, our method can be adapted to study systems other than the NPC, as long as the system has the following properties: it must be oriented with respect to a larger cellular structure, such as the plasma membrane or ordered cytoskeletal structures; a crystal structure containing a C-terminal α-helix must be known for at least one component of the system; the local concentration of the macromolecular complex must be high enough to collect data with a sufficient signal-to-noise ratio. Note that even though the NPC is a highly symmetrical structure, this is not a requirement for the application of the present method. Although the extreme C terminus of many proteins may consist of a small number of disordered residues, these residues can be trimmed to fuse the GFP to the most C-terminal α-helix, as we have demonstrated here for Nic96.

One example of a different biological system to which our method can be applied is the vacuolar ATPase system (**Supplementary Fig. 4**), and another potential example is co-translational protein translocation into the endoplasmic reticulum (ER). The rough ER is continuous with the outer nuclear envelope, which is densely covered with ribosomes engaged in co-translational protein translocation. Because the cytoplasmic-luminal axis of the protein-conducting channel-ribosome system is always perpendicular to the surface of the nuclear envelope segment to which it is attached, the average steady-state orientation of different GFP-tagged components of the system can be determined exactly as for the NPC.

METHODS

Methods and any associated references are available in the online version of the paper at http://www.nature.com/nsmb/.

Note: Supplementary information is available on the Nature Structural & Molecular Biology website.

1. Lim, R.Y., Ullman, K.S. & Fahrenkrog, B. Biology and biophysics of the nuclear pore complex and its components. *Int. Rev. Cell Mol. Biol.* **267**, 299–342 (2008).
2. Beck, M., Lucic, V., Forster, F., Baumeister, W. & Medalia, O. Snapshots of nuclear pore complexes in action captured by cryo-electron tomography. *Nature* **449**, 611–615 (2007).
3. Brohawn, S.G., Partridge, J.R., Whittle, J.R. & Schwartz, T.U. The nuclear pore complex has entered the atomic age. *Structure* **17**, 1156–1168 (2009).
4. Kampmann, M. & Blobel, G. Three-dimensional structure and flexibility of a membrane-coating module of the nuclear pore complex. *Nat. Struct. Mol. Biol.* **16**, 782–788 (2009).
5. Alber, F. *et al.* The molecular architecture of the nuclear pore complex. *Nature* **450**, 695–701 (2007).
6. Schrader, N. *et al.* Structural basis of the nic96 subcomplex organization in the nuclear pore channel. *Mol. Cell* **29**, 46–55 (2008).
7. Brohawn, S.G. & Schwartz, T.U. Molecular architecture of the Nup84–Nup145C–Sec13 edge element in the nuclear pore complex lattice. *Nat. Struct. Mol. Biol.* **16**, 1173–1177 (2009).
8. Brohawn, S.G., Leksa, N.C., Spear, E.D., Rajashankar, K.R. & Schwartz, T.U. Structural evidence for common ancestry of the nuclear pore complex and vesicle coats. *Science* **322**, 1369–1373 (2008).
9. Seo, H.S. *et al.* Structural and functional analysis of Nup120 suggests ring formation of the Nup84 complex. *Proc. Natl. Acad. Sci. USA* **106**, 14281–14286 (2009).
10. Debler, E.W. *et al.* A fence-like coat for the nuclear pore membrane. *Mol. Cell* **32**, 815–826 (2008).
11. Hsia, K.C., Stavropoulos, P., Blobel, G. & Hoelz, A. Architecture of a coat for the nuclear pore membrane. *Cell* **131**, 1313–1326 (2007).
12. Ajtai, K., Toft, D.J. & Burghardt, T.P. Path and extent of cross-bridge rotation during muscle contraction. *Biochemistry* **33**, 5382–5391 (1994).
13. Axelrod, D. Carbocyanine dye orientation in red cell membrane studied by microscopic fluorescence polarization. *Biophys. J.* **26**, 557–573 (1979).
14. Rocheleau, J.V., Edidin, M. & Piston, D.W. Intrasequence GFP in class I MHC molecules, a rigid probe for fluorescence anisotropy measurements of the membrane environment. *Biophys. J.* **84**, 4078–4086 (2003).
15. Vrabioiu, A.M. & Mitchison, T.J. Structural insights into yeast septin organization from polarized fluorescence microscopy. *Nature* **443**, 466–469 (2006).
16. Vrabioiu, A.M. & Mitchison, T.J. Symmetry of septin hourglass and ring structures. *J. Mol. Biol.* **372**, 37–49 (2007).
17. Corrie, J.E. *et al.* Dynamic measurement of myosin light-chain-domain tilt and twist in muscle contraction. *Nature* **400**, 425–430 (1999).
18. Mattheyses, A.L., Kampmann, M., Atkinson, C.E. & Simon, S.M. Fluorescence anisotropy reveals order and disorder of protein domains in the nuclear pore complex. *Biophys. J.* **99**, 1706–1717 (2010).
19. Rosell, F.I. & Boxer, S.G. Polarized absorption spectra of green fluorescent protein single crystals: transition dipole moment directions. *Biochemistry* **42**, 177–183 (2003).
20. Jeudy, S. & Schwartz, T.U. Crystal structure of nucleoporin Nic96 reveals a novel, intricate helical domain architecture. *J. Biol. Chem.* **282**, 34904–34912 (2007).
21. Berke, I.C., Boehmer, T., Blobel, G. & Schwartz, T.U. Structural and functional analysis of Nup133 domains reveals modular building blocks of the nuclear pore complex. *J. Cell Biol.* **167**, 591–597 (2004).
22. Boehmer, T., Jeudy, S., Berke, I.C. & Schwartz, T.U. Structural and functional studies of Nup107/Nup133 interaction and its implications for the architecture of the nuclear pore complex. *Mol. Cell* **30**, 721–731 (2008).
23. Whittle, J.R. & Schwartz, T.U. Architectural nucleoporins Nup157/170 and Nup133 are structurally related and descend from a second ancestral element. *J. Biol. Chem.* **284**, 28442–28452 (2009).
24. Choe, S. & Sun, S.X. The elasticity of α-helices. *J. Chem. Phys.* **122**, 244912 (2005).
25. Devos, D. *et al.* Simple fold composition and modular architecture of the nuclear pore complex. *Proc. Natl. Acad. Sci. USA* **103**, 2172–2177 (2006).
26. Melcák, I., Hoelz, A. & Blobel, G. Structure of Nup58/45 suggests flexible nuclear pore diameter by intermolecular sliding. *Science* **315**, 1729–1732 (2007).
27. Shulga, N. *et al. In vivo* nuclear transport kinetics in *Saccharomyces cerevisiae*: a role for heat shock protein 70 during targeting and translocation. *J. Cell Biol.* **135**, 329–339 (1996).

ONLINE METHODS

Yeast strains. *Saccharomyces cerevisiae* W303a and W303α cells (American Tissue Culture Collection) were transformed with the BglII fragment of pRS422 (ref. 28) containing the *ADE2* gene. Adenine-prototroph transformants were selected and crossed to obtain the diploid MKY363. Nucleoporins and Tfp1 were genomically tagged with enhanced GFP (eGFP) in MKY363 with standard methods[29], using the primers listed in **Supplementary Table 1** and the template plasmids pKT127 and pKT128 (ref. 29). The identity of the different Nic96-GFP strains was confirmed by sequencing the genomic DNA junction region between Nic96 and GFP, using the control primers listed in **Supplementary Table 1**. Sporulation and tetrad dissection of diploid cells followed standard procedures[30].

Construction of nucleoporin-GFP plasmids for expression in mammalian cells. In a first polymerase chain reaction (PCR), the eGFP coding sequence was amplified from plasmid pEGFP-C1 (Clontech) using primers GFP-f and GFP-NotI-r (**Supplementary Table 1**), introducing a NotI site downstream of the stop codon. In a second PCR, a fragment of the Nup133 coding sequence was amplified from plasmid MHS1010-58232 (Open Biosystems) and the junction with the eGFP sequence was introduced using the forward primer Nup133-f and different reverse primers for the different Nup133-GFP constructs (**Supplementary Table 1**). In a third PCR, products from the first two PCRs were used as templates with primers Nup133-f and GFP-NotI-r to fuse the Nup133 fragment to the full-length GFP sequence. The product of this PCR and plasmid MHS1010-58232 were digested with PflFI and NotI, and the PCR product was ligated into the larger background fragment from the MHS1010-58232 digest to obtain Nup133-GFP expression plasmids. The sequence of the insert was verified by sequencing with primers M13-Forward (−20), Nup133-f, Nup133-GFP-seq-1, Nup133-GFP-seq-2, and Nup133-GFP-seq-3 (**Supplementary Table 1**).

Microscopy. Images were collected on an Olympus IX-70 microscope with a 1.45-NA 60× objective lens (Olympus), using light from a 488-nm argon laser (Spectra Physics) passed through a polarizer (Chroma) and a half wave plate (ThorLabs). A 535/30ET emission filter (Chroma) and 500LP dichroic (Chroma) were used and the components of the emitted light parallel and perpendicular to the direction of polarization of the exciting light were separated by an Optosplit III splitter (Cairn) containing a polarizer (Chroma), passed through clean-up polarizers (Chroma) and simultaneously recorded side by side with an Orca ER camera (Hamamatsu). Image acquisition was software-controlled (Metamorph). *Yeast.* To minimize background fluorescence, yeast cells were grown exponentially for 24 h by sequential dilution in low-fluorescence medium[29] at 30 °C. For imaging, diploid cells from 1–3 ml of culture were resuspended in a small amount of low-fluorescence medium, 1 μl was dispensed onto a glass slide, and a cover slip (Number 1.5, VWR) was applied with slight pressure. Images were collected at 20 °C with 2,000-ms exposure time.

Mammalian cells. HeLa cells were grown in DMEM (GIBCO) containing penicillin, streptomycin and FBS (GIBCO) in 35-mm glass bottom dishes (No. 1.5, MatTek). Cells were transfected with Nup133-GFP expression plasmids using Lipofectamine (Invitrogen), following the manufacturer's protocol. Cells were imaged 18–48 h after transfection in Hank's balanced salt solution (Sigma) containing 5% FBS and 10 mM HEPES buffer, pH 7.4, at 37 °C, with 2,000 ms exposure time.

Computational image analysis. *Background subtraction.* Images of cells were corrected for growth-medium fluorescence by subtracting an image of the medium. Images of individual nuclei were cropped from micrographs, and the cytoplasmic background for each cell was subtracted.

Anisotropy compensation. The difference in light transmission between the parallel and perpendicular channels was corrected using images of aqueous fluorescein solution (Sigma), for which we assumed an anisotropy of 0. We applied objective correction factors developed previously (ref. 13 and **Supplementary Note**).

Image alignment. Images from the parallel and perpendicular channels were aligned with sub-pixel accuracy based on cross-correlation in SPIDER[31].

Yeast. The remaining processing steps were implemented in Matlab (The Mathworks). An anisotropy image was calculated from the aligned parallel and perpendicular images according to the definition of anisotropy (equation (1)). To mask pixels outside the nuclear envelope, only the 10% brightest pixels in a sum image of the parallel and perpendicular channels were included in further analysis. The image was divided in 32 sectors, each corresponding to an angle of 11.25°, the average anisotropy was calculated for all pixels from all cells falling within each sector, and the s.d. was calculated for at least 75 cells per construct.

Mammalian cells. 16 × 16 pixel images of nuclear envelope segments were cropped from micrographs. In SPIDER, the cross-correlation was calculated between these segments and 18 artificial images of a line with different orientations, as shown in **Figure 5d**. Each image was assigned to the most similar template. Only pixels with intensities at least 1 s.d. above the average pixel intensity were included in the further analysis. The average anisotropy was calculated for each image. For all images aligned to one template, the average anisotropy and s.d. were calculated (a minimum of 500 boxes per construct translated to ~25–30 boxes per anisotropy value).

Molecular models. Models of fusion proteins were built in UCSF Chimera[32] from the following crystal structures: eGFP, PDB 1EMG[33]; Nic96, PDB 2QX5 (ref. 20); Nup133–Nup107, PDB 3I4R[23]; Tfp1, PDB 1VDZ[34]. GFP was positioned with respect to the tagged protein such that the linker helix was continuous. Vectors were calculated from PDB coordinates: μ, vector between fluorophore atoms CE1 and O2; Nic96-u, vector between Trp334-CA and Ile723-CG1; Nic96-v, vector normal to Nic96-u passing through Leu200-N; Nup133-Nup107-u, vector between Nup107-Glu667-CA and Nup133-Lys518-CA; Nup133-Nup107-v, vector normal to Nup133-Nup107-u passing through Nup133-Ile1156-CA; Tfp1-u, vector between Val521-C and Gln191-OE1. Angles θ and ω for each construct were calculated from these vector coordinates. Maps of α as a function of φ and ψ were calculated in Matlab as detailed in the **Supplementary Note**. The following EM structures were used: EMDB-5152 (ref. 4) for **Figure 6c** and **Supplementary Figure 6**; EMDB-1640 (ref. 35) for **Supplementary Figure 4**. Registration of the yeast Tfp1 sequence with PDB 1VDZ was determined using FUGUE[36].

28. Brachmann, C.B. *et al.* Designer deletion strains derived from *Saccharomyces cerevisiae* S288C: a useful set of strains and plasmids for PCR-mediated gene disruption and other applications. *Yeast* **14**, 115–132 (1998).
29. Sheff, M.A. & Thorn, K.S. Optimized cassettes for fluorescent protein tagging in *Saccharomyces cerevisiae*. *Yeast* **21**, 661–670 (2004).
30. Sherman, F. Getting started with yeast. *Methods Enzymol.* **350**, 3–41 (2002).
31. Frank, J. *et al.* SPIDER and WEB: processing and visualization of images in 3D electron microscopy and related fields. *J. Struct. Biol.* **116**, 190–199 (1996).
32. Pettersen, E.F. *et al.* UCSF Chimera—a visualization system for exploratory research and analysis. *J. Comput. Chem.* **25**, 1605–1612 (2004).
33. Elsliger, M.A., Wachter, R.M., Hanson, G.T., Kallio, K. & Remington, S.J. Structural and spectral response of green fluorescent protein variants to changes in pH. *Biochemistry* **38**, 5296–5301 (1999).
34. Maegawa, Y. *et al.* Structure of the catalytic nucleotide-binding subunit A of A-type ATP synthase from *Pyrococcus horikoshii* reveals a novel domain related to the peripheral stalk. *Acta Crystallogr. D Biol. Crystallogr.* **62**, 483–488 (2006).
35. Diepholz, M. *et al.* A different conformation for EGC stator subcomplex in solution and in the assembled yeast V-ATPase: possible implications for regulatory disassembly. *Structure* **16**, 1789–1798 (2008).
36. Shi, J., Blundell, T.L. & Mizuguchi, K. FUGUE: sequence-structure homology recognition using environment-specific substitution tables and structure-dependent gap penalties. *J. Mol. Biol.* **310**, 243–257 (2001).